Available online at www.sciencedirect.com
SCIENCE DIRECT®
International Journal of Heat and Fluid Flow 25 (2004) 897–914
International Journal of HEAT AND FLUID FLOW
www.elsevier.com/locate/ijhff

The turbulent flow in an enclosed corotating disk pair: axisymmetric numerical simulation and Reynolds stress modelling

A. Randriamampianina [a,*], R. Schiestel [a], M. Wilson [b]

[a] Institut de Recherche sur les Phénomènes Hors Equilibre, UMR 6594 CNRS, Technopôle de Château-Gombert. 49, rue F. Joliot Curie, BP 146, 13384 Marseille Cedex 13, France
[b] Department of Mechanical Engineering, Faculty of Engineering and Design, University of Bath, Bath BA2 7AY, UK

Received 6 June 2003; accepted 24 March 2004
Available online 7 June 2004

Abstract

We present axisymmetric numerical simulation and modelling of the turbulent flow between corotating disks with a stationary outer casing, the enclosed corotating disk pair configuration. This follows previous work on laminar flow for an identical geometry defined by a gap ratio $G = 0.6$ $(= s/(b-a))$ and $a/b = 0.5$, where a and b are the inner and outer radii, and s is the inter-disk distance [J. Fluid Mech. 434 (2001) 39]. The rotation rate considered in the present case is equivalent to $Re = 1.46 \times 10^5$, where Re $(= \Omega b^2/v)$ is the rotational Reynolds number. This corresponds to a value at which mean flow measurements have been obtained for the same configuration [Flow in a rotating cavity with a peripheral inlet and outlet of cooling air, in: ASME Int. Gas Turbine and Aeroengine Cong., paper 96-GT-309, Birmingham]. In computed laminar regimes, it was found previously for this aspect ratio that the flow structure is first characterized by a shift-and-reflect symmetry at lower values of Re before bifurcating to symmetry breaking at higher rotation rates. For the rotation rate under consideration here, the flow is turbulent and shows an unsteady behaviour in the mean, characterized by flapping of the flow between the two disks, inducing symmetry breaking with respect to the inter-disk midplane. Similarities are observed between the centripetal flow coming from the stationary casing and an impinging jet in a cavity. Comparisons are made between the computed results from the axisymmetric numerical simulation (ANS), a Reynolds Stress Transport Model (RSM) and the available experimental data. The RSM predictions are in close agreement with the mean flow measurements. The ANS results give a more detailed description of the flow characteristics, but suffer from the axisymmetry assumption which is not compatible with the three-dimensional turbulence.

Keywords: Rotating flow; Turbulence; Numerical simulations; Modelling

1. Introduction

The Enclosed Corotating Disk Pair (ECDP) configuration is formed by two corotating disks delimited by an inner cylinder, the hub, corotating with the disks and an outer, stationary casing. The geometry considered here is characterized by a large hub outer radius ratio: $a/b = 0.5$. Applications include mainly computer disk storage systems and disk cavities in some gas turbine engines.

The present numerical study is concerned with the behaviour of the turbulent flow observed at $Re = 1.46 \times 10^5$ for $G = 0.6$, corresponding to the lowest value of the rotation rate at which mean flow measurements have been obtained at the University of Bath (Gan et al., 1996).

In experiments with air, Schuler et al. (1990) delineated five distinct flow regions (illustrated in Fig. 1) for values of the rotational Reynolds number $2.22 \times 10^4 \leqslant Re \leqslant 2.66 \times 10^5$ with $G = 0.196$ and $a/b = 0.537$: the region near the hub driven by solid-body rotation (denoted region IV), the boundary layer close to the stationary casing or shroud (region I), the inviscid core (region II) characterized by negligible gradients of the velocity components in the radial and axial directions, region III corresponding to the transition between regions II and IV, and the Ekman-type boundary layers along the two disks (region V). The core region is

* Corresponding author.
E-mail address: anthony.randria@irphe.univ-mrs.fr (A. Randriamampianina).

0142-727X/$ - see front matter © 2004 Elsevier Inc. All rights reserved
doi:10.1016/j.ijheatfluidflow.2004.03.003

Nomenclature

a	inner radius
b	outer radius
C_w	dimensionless mass flowrate $\dot{m}/\mu b$
C_{ij}	structure parameter of turbulence
G	aspect ratio $s/(b-a)$
k	turbulent kinetic energy
$\bar{k}$	time mean kinetic energy
k'	fluctuating turbulent kinetic energy
$\overbrace{k}$	total kinetic energy
$\dot{m}$	mass flowrate in the half of the cavity
P	pressure
r	radius
Re	rotational Reynolds number $\Omega b^2/\nu$
Re_T	turbulent Reynolds number
R_c	curvature parameter $(a+b)/(b-a)$
R_{ij}	turbulent Reynolds stress tensor
$\overline{R_{ij}}$	time mean value of the turbulent Reynolds stress tensor $\overline{u_i' u_j'}$
R'_{ij}	fluctuating Reynolds stress tensor
$\widetilde{R_{ij}}$	pseudostress tensor $\overline{\widetilde{u_i}\widetilde{u_j}}$
$\overbrace{R_{ij}}$	apparent stress tensor
s	distance between corotating disks
T_m	Chebyshev polynomial of degree m
U_j	velocity vector
$\langle U_j \rangle$	phase-averaged velocity vector
$\widetilde{u_j}$	organized macrocomponent of velocity
u'_j	turbulent fluctuating velocity
x	reduced radius r/b
y	reduced axial coordinate z/s
z	axial coordinate

Greeks

θ	azimuthal coordinate
ζ	vorticity
η	Kolmogorov scale
ρ	density
μ	dynamic viscosity
ν	kinematic viscosity
κ_j	wavevector in spectral space
Ω	rotation speed

Operators

$\langle \Phi \rangle$	phase average of Φ
$\overline{\Phi}$	time mean value of Φ
$\widetilde{\Phi}$	organized fluctuation of Φ: $\overline{\Phi} - \langle \Phi \rangle$
Φ'	turbulent fluctuation of Φ: $\langle \Phi \rangle - \Phi$

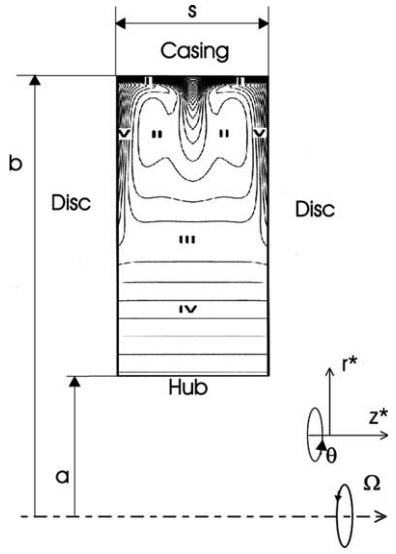

Fig. 1. Schematic diagram of the ECDP section with relevant dimensions and definition of the five regions in the (r,z) plane (based on Schuler et al., 1990).

composed of two separate zones in the meridional (r–z) plane, which may or may not exhibit symmetry with respect to the inter-disk midplane. Region III (visualized by Abrahamson et al. (1989) as a polygon in the (r,θ) plane) constitutes a detached shear layer, resulting from the meeting of the three-dimensional vortical structures in region II with the two-dimensional flow in region IV (which satisfies the Taylor–Proudman theorem). This separation is found to act like a compliant surface, with the presence of a critical radius where the azimuthal angular velocity peaks. Exchange between the two regions II and IV occurs via spiral arms (see Akhmetov and Tarasov, 1987; Randriamampianina et al., 2001). Schuler et al. (1990) also analysed the different scales of the flow dynamics in each region. On the other hand, from their experiments with water as the working fluid, Abrahamson et al. (1989) reported that the "inner and outer regions are very two-dimensional, with little variation in the direction parallel to the spin axis. The shroud boundary layer region was more three-dimensional". For a fixed gap ratio, they observed the occurrence of three flow regimes with increasing rotation rate: indeterminate, alternating vortex states and stable vortices. They also mentioned that the number of outer vortices tends to decrease when the rotation rate increases, and emphasized the presence of intransitivity ("the flow can exist in a number of states at any given disk speed"), although a predominant state could be obtained.

Experimental and computational studies have been carried out at the University of Bath (Gan et al., 1996; Mirzaee et al., 1997) for the present configuration

($G = 0.6$), at high rotation rates leading to turbulent flows. In particular, Gan et al. (1996) identified a Rankine (combined free and forced) vortex structure for the measured mean flow (see also Owen and Rogers, 1995, for a review of flow and heat transfer in rotating cavities). Dependence upon radial location of the local rotation rate of the flow in *rotor–stator* systems has been reported both experimentally (Gauthier et al., 1999) and numerically (Randriamampianina et al., 1997). The main difference in the present configuration comes from the characteristic behaviour in the different regions, in particular the variation as a Rankine vortex with the presence of an inner detached shear layer.

In this paper, numerical simulations are performed for axisymmetric flow regimes; extension to fully three-dimensional calculations will be described in the future. Such a strategy has been applied successfully in a previous study of the Ekman boundary layer instability in rotating cavities with a superposed throughflow (Crespo del Arco et al., 1996). These axisymmetric solutions were able to give correct prediction of the threshold for the instability compared with data available in the literature, and to capture the main features of the unsteady flow. The results were confirmed later by full three-dimensional computations (Hugues et al., 1998; Serre et al., 2001). It is inferred that this approach will be also useful in turbulent regimes. Indeed, Coleman et al. (1990) observed that "the turbulent Ekman layer has more in common with the turbulent two-dimensional boundary layer than with the quasi-laminar Ekman layer (due especially to the lack of longitudinal rolls)". Moreover, axisymmetric propagating vortices, visualized as circular rolls, have been observed in recent experiments in rotating disk systems (Gauthier et al., 1999; Schouveiler et al., 2001). Numerical simulation, which produces the time-dependent evolution of the flow field, gives a detailed description of flow structures, their geometrical extent and unsteadiness and also permits statistical treatment providing mean values, correlations and spectra.

For the present configuration (see Randriamampianina et al., 2001), it was found that axisymmetric solutions exist at low rotation rates, initially showing symmetry with respect to the inter-disk midplane, before undergoing a pitchfork bifurcation characterized by a breaking of this symmetry (see also Herrero et al., 1999). Further increase in rotation rate yields a Hopf bifurcation, where the oscillatory motion is induced by a flapping between the two disks of the centripetal flow from the stationary casing. For the rotational Reynolds number considered in the present study, $Re = 1.46 \times 10^5$, the flow is found to be turbulent. However, the mean flow exhibits unsteady behaviour, similar to the phenomenon described above during the Hopf bifurcation; similarity with an impinging jet in a cavity is observed and discussed below. Other results, based on one-point statistical modelling with a low-Reynolds number, second-order, stress-transport closure (RSM), are also produced for the present problem, and comparisons of the mean flow with available measurements from Gan et al. (1996) are carried out.

The characteristics of the turbulence field in systems subjected to high rotation rates are very specific. Rotation not only inhibits the inertial cascade process but modifies the structural properties of the turbulence field (see Cambon and Jacquin, 1989). Advanced turbulence closures are thus necessary to handle such types of flows (see Elena and Schiestel, 1996). The flow is particularly complex due to the occurrence of strong shear within the very thin Ekman layer region along the disk and also near the upper corners formed by the periphery of the disks and the stationary casing. As a consequence, the turbulence field reaches high intensities in these regions, while laminarized zones prevail in the inner part of the cavity towards the rotating hub (resulting from the Taylor–Proudman theorem).

The main objective of this work is to study the structure and properties of the flow developing in the enclosed corotating disk pair, and in particular the oscillating jet-like structure originating from the stationary outer casing. The numerical simulation is a first approach based on the axisymmetry hypothesis that will be extended to a full three-dimensional description in the future. At the present time, it is interesting to analyze to what extent the axisymmetric computations could contribute to an understanding of this kind of complex flow.

The experimental rig used by Gan et al. (1996) is described in Section 2. The mathematical models and solution methods for the axisymmetric numerical simulation and the turbulent prediction are given respectively in Sections 3 and 4. Results and discussion are provided in Sections 5 and 6, where comparisons of the mean flow with available measurements from Gan et al. (1996) are discussed. Concluding remarks appear in Section 7.

2. Details of the experimental rig

A full description of an ECDP experimental rig and test programme was given by Gan et al. (1996) and Mirzaee et al. (1997); details relevant to sealed cavity experiments are summarized here. The disks were $2b = 762$ mm in diameter and were separated by a distance $s = 113$ mm with an inner cylinder of diameter $2a = 381$ mm, giving a gap ratio $G = s/(b - a) = 0.6$ and radius ratio $a/b = 0.5$. The working fluid was air at atmospheric pressure and temperature, and the rotation rate considered in the present study corresponds to $\Omega = 15.7$ rd/s. Separate measurements of radial and tangential velocities were made at selected axial and

radial locations, using a transparent disk for optical access and backscatter laser doppler anemometry. The positional uncertainty of the optical probe volume was 0.13 mm and the uncertainty in individual velocity measurements was estimated as ±3%.

3. Mathematical model and solution method for the axisymmetric numerical simulation (ANS)

3.1. Governing equations

The instantaneous motion is governed by the Navier–Stokes equations for incompressible fluids. With the axisymmetry assumption, the formulation in stream-function ψ and vorticity ζ is preferred to primitive variables, reducing the number of equations to be solved and satisfying the mass conservation irrespective of the resolution considered. The definitions of ψ and ζ are as follows:

$$\zeta = \frac{\partial U_r}{\partial z} - \frac{\partial U_z}{\partial r} \tag{3.1}$$

$$U_r = \frac{1}{r}\frac{\partial \psi}{\partial z}, \quad U_z = -\frac{1}{r}\frac{\partial \psi}{\partial r} \tag{3.2}$$

where (U_r, U_θ and U_z) are the velocity components in a stationary frame of reference in the radial, azimuthal and axial directions respectively.

The space variables are normalized into the square $[-1,1]\times[-1,1]$, a prerequisite for the use of Chebyshev polynomials (see Fig. 1, dimensionless variables are marked with a star):

$$r^* = \frac{2r-b-a}{b-a} \quad \text{and} \quad z^* = \frac{2z}{s} - 1$$

Characteristic time and velocity scalings are $t_{\text{ref}} = s/2b\Omega$ and $U_{\text{ref}} = \Omega b$ respectively.

In a stationary frame of reference, the resulting dimensionless system is (with the * notation dropped):

$$\frac{\partial U_\theta}{\partial t} + GU_r\frac{\partial U_\theta}{\partial r} + U_z\frac{\partial U_\theta}{\partial z} + G\frac{U_rU_\theta}{r+R_c} = \frac{R_c+1}{GRe}\Delta U_\theta \tag{3.3}$$

$$\frac{\partial \zeta}{\partial t} + GU_r\frac{\partial \zeta}{\partial r} + U_z\frac{\partial \zeta}{\partial z} - G\frac{U_r\zeta}{r+R_c} = 2G\frac{U_\theta}{r+R_c}\frac{\partial U_\theta}{\partial z} + \frac{R_c+1}{GRe}\Delta\zeta \tag{3.4}$$

$$G^2\frac{\partial^2\psi}{\partial r^2} - G^2\frac{1}{r+R_c}\frac{\partial \psi}{\partial r} + \frac{\partial^2\psi}{\partial z^2} = (r+R_c)\zeta \tag{3.5}$$

where Δ is the dimensionless Laplacian operator:

$$\Delta = G^2\left(\frac{\partial^2}{\partial r^2} + \frac{1}{r+R_c}\frac{\partial}{\partial r} - \frac{1}{(r+R_c)^2}\right) + \frac{\partial^2}{\partial z^2}$$

The characteristic parameters governing the motion are: the rotational Reynolds number, $Re = \Omega b^2/\nu$; the cavity aspect ratio, $G = s/(b-a)$; the curvature parameter, $R_c = (a+b)/(b-a)$.

The boundary conditions for the vorticity are derived directly from Eq. (3.5), and using the no-slip conditions at rigid walls (Randriamampianina et al., 1986; Randriamampianina et al., 1987):

$$\zeta_w = G^2\left(\frac{1}{r+R_c}\frac{\partial^2\psi}{\partial n^2}\right)_w$$

where n is the normal direction.

The inner cylinder and the two disks rotate with the same angular velocity Ω, while the outer cylinder is stationary. However, in order to maintain the spectral accuracy of the solution, a regularization is introduced for the tangential velocity component at the corner discontinuity between the disks and the casing:

$$U_\theta = U_{\theta 0}(r) \tag{3.6}$$

where $U_{\theta 0}(r) = (R_c+r)(1-\exp(A_r(1-r)))/(R_c+1)$; A_r is a constant (see Randriamampianina et al., 1997), chosen to allow a small radial clearance δ between the disk and the casing such that $\delta/b < 0.02$ (see also Tavener et al., 1991; Randriamampianina et al., 2001).

3.2. Temporal scheme

The time integration used is second order accurate and is based on a combination of Adams-Bashforth and Backward Differentiation Formula schemes, chosen for its good stability properties (Vanel et al., 1986). The resulting AB/BDF scheme is semi-implicit, and for the transport equation of any dependent variable f ($f = \zeta, U_\theta$) can be written as

$$\frac{3f^{l+1} - 4f^l + f^{l-1}}{2\delta t} + 2\mathcal{N}(f^l) - \mathcal{N}(f^{l-1}) = \frac{(R_c+1)}{GRe}\Delta f^{l+1} \tag{3.7}$$

where $\mathcal{N}(f)$ stands for nonlinear terms, n is the normal direction, δt the time step and the superscript l refers to time level. For the initial step, we have taken $f^{-1} = f^0$.

At each time step, the problem then reduces to the solution of Helmholtz and Poisson equations.

3.3. Numerical approach and computational details

The spatial approximation is based on a pseudo-spectral collocation-Chebyshev technique. Each dependent variable f is expanded in the approximation space P_{NM}, composed of Chebyshev polynomials of degrees less than or equal to N and M respectively in the radial (r) and axial (z) directions:

$$f_{NM}(r,z,t) = \sum_{n=0}^{N}\sum_{m=0}^{M}\hat{f}_{nm}(t)T_n(r)T_m(z)$$

where $(r,z) \in [-1,1] \times [-1,1]$ and T_n and T_m are Chebyshev polynomials of degrees n and m.

This approximation is applied at collocation points, where the differential equations are assumed to be satisfied exactly (Gottlieb and Orszag, 1977; Canuto et al., 1987). We have considered the Chebyshev–Gauss–Lobatto points, corresponding to the extrema of the Chebyshev polynomials of highest degrees, say N and M: thus $x_i = \cos(\frac{i\pi}{N})$ for $i \in [0,N]$ and $y_j = \cos(\frac{j\pi}{M})$ for $j \in [0,M]$.

The numerical approach is based on an influence matrix technique introduced to treat the lack of boundary conditions for the vorticity (Chaouche et al., 1990). A complete diagonalization of operators yields simple matrix products for the solution of successive Helmholtz and Poisson equations at each time step (Haldenwang et al., 1984). The computations of eigenvalues, eigenvectors and inversion of corresponding matrices are performed once during a preprocessing step.

A grid resolution $N \times M = 180 \times 128$ in the radial and axial directions with a non-dimensional time step $\delta t = 10^{-4}$ was used for the computations. A grid test with a finer resolution $N \times M = 200 \times 150$ (associated with the more severe numerical stability constraint $\delta t = 6.25 \times 10^{-5}$) did not produce significant changes in the flow features.

From the physical point of view, the mesh must be chosen in order to capture all the scales present in the flow. An estimate of the size of the smallest dissipative eddies, known as the Kolmogorov scale, has been made from statistical modelling results that produce the viscous dissipation rate ϵ:

$$\frac{\eta}{s} = \frac{v^{3/4}}{s\epsilon^{1/4}}$$

An a posteriori estimate of a value obtained from modelling (RSM) results for the Ekman layer gives $\eta/s \approx 0.01$ outside the viscous sublayer, which is satisfied along the rotating disk by the present resolution. Very small scales develop within these boundary layers where the turbulence originates. This was not the case towards the centre of the cavity, where a coarser grid results from the Gauss–Lobatto–Chebyshev distribution. However, since larger scales are expected to prevail in these central regions, we believe that the resolution considered is sufficient to produce correct behaviour for these largest eddies and for the mean flow, which is a goal of the present study.

Another point that can be influential is the axisymmetry hypothesis which leads to a form of two-dimensional turbulence, in which the Kolmogorov scale restriction is less crucial. Indeed, according to Lesieur (1990), if energy is injected at a wavenumber κ_I in two-dimensional turbulence, an enstrophy cascade $\beta = \kappa_I^2 \epsilon$ will take place at high wavenumbers along with the inverse energy cascade at low wavenumbers. The dissipative scale of the enstrophy cascade is given by $\kappa_D = \beta^{1/6}/v^{1/2}$ and if we suppose $\epsilon \approx k^{3/2}\kappa_I$ this implies that $\ell_D = \kappa_D^{-1} \approx \eta Re_T^{1/4}$ ($Re_T = k^2/v\epsilon$). When the turbulence Reynolds number exceeds unity the dissipative scale is larger than the Kolmogorov scale, and the condition is less severe.

3.4. The axisymmetry assumption in the numerical simulation

The axisymmetry hypothesis allows a huge economy of computer storage and processor time. Considering also that a statistical treatment requires long time averaging, this practical constraint will be used in the present approach. It is important, however, to discuss the physical consequences of such an assumption.

It is well known that the two-dimensional hypothesis inhibits the vortex-stretching phenomenon which controls the energy cascade in three-dimensional turbulence, even though stretching of vorticity gradients is present. In this respect, therefore, the mechanisms involved in two-dimensional turbulence are different from those prevailing in more common turbulence (see Lesieur, 1990). However, it is worthwhile to note that such two-dimensionality does not imply that U_θ is zero in the present situation. Consequently the turbulence intensity $\overline{u_\theta'^2}$ is nonzero, as it would be the case in a two-component planar flow. In other words, the turbulence field is two-dimensional but not "two-componental" (this is a different concept, see Kassinos et al., 2001). Indeed, in the present computations, the $\overline{u_\theta'^2}$ is of the same order of magnitude as the two other components $\overline{u_r'^2}$ and $\overline{u_z'^2}$. The axisymmetry assumption implies just that the turbulence spectrum in the azimuthal direction is concentrated in a Dirac distribution. Also, it seems logical to suggest that the breaking of the inertial cascade process will have more limited consequences if the Reynolds number is not too high.

It should also be noted that vortex stretching by the mean flow is still present in the case of axisymmetry; toroidal vortices can be stretched by centrifugal velocity components. Further point to mention is that, if the usual mechanisms of turbulence production in a classical three-dimensional boundary layer are not relevant in the present case, turbulence production is still not suppressed. Thus, it appears that the axisymmetry hypothesis is useful for a first approach. This was also the conclusion of the work of Jacques et al. (2002) who successfully carried out axisymmetric simulations of turbulence in a rotor–stator enclosure.

Another consequence of the axisymmetry hypothesis is that the pressure–strain correlation in the $\overline{u_\theta'^2}$ equation is zero, so that the return to isotropy process is suppressed in this direction. Thus, higher levels of

anisotropy may be expected. The consequences for the turbulence field are clearly interpreted from the structural anisotropy, $C_{\theta\theta} = 0$, according to the definition given by Kassinos et al. (2001) and Cambon et al. (1992) in homogeneous turbulence:

$$C_{ij} = \int \frac{\kappa_i \kappa_j}{\kappa^2} \mathscr{E}(\vec{\kappa}) \mathrm{d}(\vec{\kappa})$$

where $\mathscr{E}(\vec{\kappa})$ corresponds to the energy spectrum and $\vec{\kappa} \equiv (\kappa_i)$ is the wavevector. This is true, however, only in homogeneous turbulence and in the present case the confinement by the lateral walls tends to break this structural tendency. Further, the axisymmetry hypothesis on the instantaneous field obviously does not involve axisymmetry of the turbulent stresses. Turbulence axisymmetry is a different concept which would imply that locally two eigenvalues of the Reynolds stress tensor are equal (see Chasnov, 1995); this is not the case here.

These remarks suggest that, although some important features of the flow will be altered by the axisymmetry assumption, the numerical simulation can produce useful initial results, as in Jacques et al. (2002). Another argument for the usefulness of such calculations is the presence, as already mentioned in the Introduction, of the propagating circular axisymmetric rolls observed in experiments that are believed to be characteristic structures of the flow near a rotating disk.

4. Mathematical model and numerical method for turbulent flow prediction (RSM)

4.1. Governing equations

For turbulent mean flow prediction, the governing equations for the conservation of mass and momentum are deduced by statistical averaging from the Navier–Stokes equations using the Reynolds decomposition: the instantaneous velocity (and respectively pressure) is decomposed into a mean part $\langle U_i \rangle$ ($\langle P \rangle$) and a fluctuating part u_i' (p'):

$$\begin{cases} \frac{\mathrm{d}\langle U_i \rangle}{\mathrm{d}t} = -\left(\frac{\langle P \rangle}{\rho}\right)_{,i} + \left(\nu \langle U_i \rangle_{,j} - R_{ij}\right)_{,j} \\ \langle U_j \rangle_{,j} = 0 \end{cases} \tag{4.1}$$

with $R_{ij} = \langle u_i' u_j' \rangle$ where $\langle \cdot \rangle$ denotes statistical ensemble average.

In order to close this system, a differential or Reynolds stress model (RSM) is used. This approach is also commonly referred to as unsteady Reynolds-averaged Navier–Stokes (URANS) model. The transport equations for the Reynolds stress tensor can be written as

$$\frac{\mathrm{d}R_{ij}}{\mathrm{d}t} = P_{ij} + D_{ij}^{\mathrm{T}} + \Phi_{ij} - \epsilon_{ij} + \nu R_{ij,mm} \tag{4.2}$$

where P_{ij}, D_{ij}^{T}, Φ_{ij} and ϵ_{ij} respectively denote the production, turbulent diffusion, pressure–strain correlation, and dissipation terms. These last three processes require modelling since they involve unknown correlations. Second order closures present distinct advantages for modelling complex turbulent flows involving extra phenomena such as an imposed rotation.

4.2. Outline of the differential Reynolds stress model

The model used in the present study is described fully in Elena and Schiestel (1996) and Schiestel and Elena (1997) (see also Randriamampianina et al., 1997). It is derived from the Launder and Tselepidakis model (Launder and Tselepidakis, 1994), and its main characteristics are summarized below. The full equations are given in Appendix A.

- In a classical way, the pressure–strain term is split into three parts:

$$\Phi_{ij} = \Phi_{ij}^{(1)} + \Phi_{ij}^{(2)} + \Phi_{ij}^{(w)}$$

The contribution $\Phi_{ij}^{(1)}$ is interpreted as a nonlinear return to isotropy and is modelled as a quadratic development in the stress anisotropy tensor, with coefficients sensitized to the invariants of anisotropy. In particular the flatness parameter $A = 1 - \frac{9}{8}(A_2 - A_3)$ is introduced, where A_2 and A_3 are the second and the third invariants of anisotropy.

A very weak turbulent region prevails in the lower (inner) part of the cavity away from the wall, and the modelling functions proposed by Launder and Tselepidakis (1994) lead to realizability problems (Elena, 1994). The damping functions used in the model equations were modified by Elena and Schiestel (1996) to overcome the problems encountered in relaminarized regions far from the wall. These modifications have been shown to be satisfactory for various confined flows (Elena, 1994).

The linear part of the pressure–strain correlation is modelled using the classical form proposed by Gibson and Launder (1978). However, the widely adopted length scale $k^{3/2}/\epsilon$ is replaced by $k(R_{ij}n_i n_j)^{1/2}/\epsilon$, which is the length scale of the fluctuations normal to the wall. Since the nonlinear slow part of the pressure–strain correlation is already damped near the wall, a wall correction is only applied to the linear rapid part.

The following further details are noted:

- The classical (Daly and Harlow, 1970) form for the turbulent diffusion term, which is interpreted as the diffusion due to both velocity and pressure fluctuations, has been used here. The viscous diffusion is retained since it cannot be neglected in the low-Reynolds number region.

- The behaviour of the viscous dissipation tensor ϵ_{ij} of the Reynolds stresses has been modelled in order to conform with the wall limits obtained from Taylor series expansions of the fluctuating velocities (Launder and Reynolds, 1983).
- The coefficients in the ϵ equation are also sensitized to the anisotropy invariants.
- The extra terms involving directional anisotropy introduced in Elena and Schiestel (1995a) and Schiestel and Elena (1997) have only a weak effect in the present application.

4.3. Numerical method

This part of the numerical investigation was carried out using a computer code developed from an adapted version of the UMIST finite volume code TEAM. In order to overcome severe stability problems associated with high rotation rates, several stabilizing techniques were introduced in the numerical procedure, such as those proposed by Huang and Leschziner (1985).

The code was extended to unsteady flows using first order time discretization with internal iterations. The solution of the six Reynolds stress components was obtained by a block tridiagonal algorithm, rather than the pointwise block resolution technique described by Elena and Schiestel (1995b,c) for an earlier (steady-state) version of the code.

4.4. Boundary conditions and grid arrangement

Owing to the use of low-Reynolds number models, no specialized treatment is needed at the boundaries. All the variables are set to zero at walls except $\langle U_\theta \rangle$ and ϵ. The dissipation rate ϵ is assigned the exact limit, $2\nu(\partial k^{1/2}/\partial n)^2$.

The use of a low-Reynolds number turbulence model requires a very fine mesh near walls in order to take into account the strong variations of the different variables. The mesh was built according to geometrical series variations. Grid dependence studies resulted in the use of a 158×198 mesh in the axial and radial directions respectively.

5. Results

Some definitions are required before the presentation of results.

The instantaneous velocity is split into a three term decomposition (see Reynolds and Hussain, 1972):

$$U_i = \overline{U_i} + \widetilde{u_i} + u_i' \quad \text{for } i \equiv r, \theta, z$$

where $\overline{U_i}$ is the time-averaged mean velocity, $\widetilde{u_i}$ corresponds to the unsteady organized macrocomponent and u_i' to the turbulent fluctuation. The total fluctuation is then

$$v_i = \widetilde{u_i} + u_i'.$$

The macrocomponent is defined from a statistical ensemble average and can be obtained for instance by a phase average (as long as periodic behaviour is reached):

$$\langle U_i \rangle = \overline{U_i} + \widetilde{u_i}.$$

Assuming that $\widetilde{u_i}$ and u_i' are uncorrelated, the total apparent stresses are

$$\overbrace{R_{ij}} = \overline{v_i v_j} = \overline{\widetilde{u_i}\widetilde{u_j}} + \overline{u_i' u_j'} \tag{5.1}$$

where $\overline{\widetilde{R_{ij}}} = \overline{\widetilde{u_i}\widetilde{u_j}}$ is a pseudostress tensor due to macrocomponents and $\overline{R_{ij}} = \overline{u_i' u_j'}$ is the time mean value of the true turbulent Reynolds stress.

The simulation produces the instantaneous values of velocity. Statistical treatment in time gives $\overline{v_i v_j}$, while the determination of turbulent stresses requires the splitting of v_i into $\widetilde{u_i}$ and u_i'. Considering the limited duration of the simulation, phase averaging is not practicable: we have obtained here $\langle v_i \rangle = \widetilde{u_i}$ as a time mean value over a short interval of time. The numerical modelling gives instantaneous values of $\langle U_i \rangle$ and $\langle u_i' u_j' \rangle$ directly; $\overline{U_i}$ and $\overline{u_i' u_j'}$ are then obtained through a long time average. Use of short time averages instead of true phase averages introduces some loss of accuracy, but it is not very significant as the frequency of the jet flapping is very low compared with the rotation speed.

It is worthwhile to point out some fundamental differences between the two approaches. The simulation is based on the hypothesis of axisymmetry of the instantaneous velocities; the tangential velocity is allowed to fluctuate but $\partial/\partial\theta \equiv 0$. This assumption impedes all three-dimensional interaction mechanisms in turbulent flows, such as three-dimensional vortex stretching. In the RSM calculation, the axisymmetry hypothesis affects only the ensemble averaged quantities. The turbulent fluctuations are still modelled using three-dimensional closure hypotheses. These remarks should be kept in mind when comparing numerical results.

5.1. Time mean flow

The time mean flow field and the isocontours of the tangential velocity component obtained from the axisymmetric numerical simulation (ANS) and the RSM are shown in Fig. 2.

Symmetry of the mean flow with respect to the inter-disk midplane is observed. The five regions described by Schuler et al. (1990) (see Fig. 1) can be identified from the isovalues of the mean tangential velocity component. The core region II, characterized by the occurrence of two large vortices, spreads over about two thirds of the cavity for the ANS, while the predicted recirculation zone is larger in the case of the RSM results, in

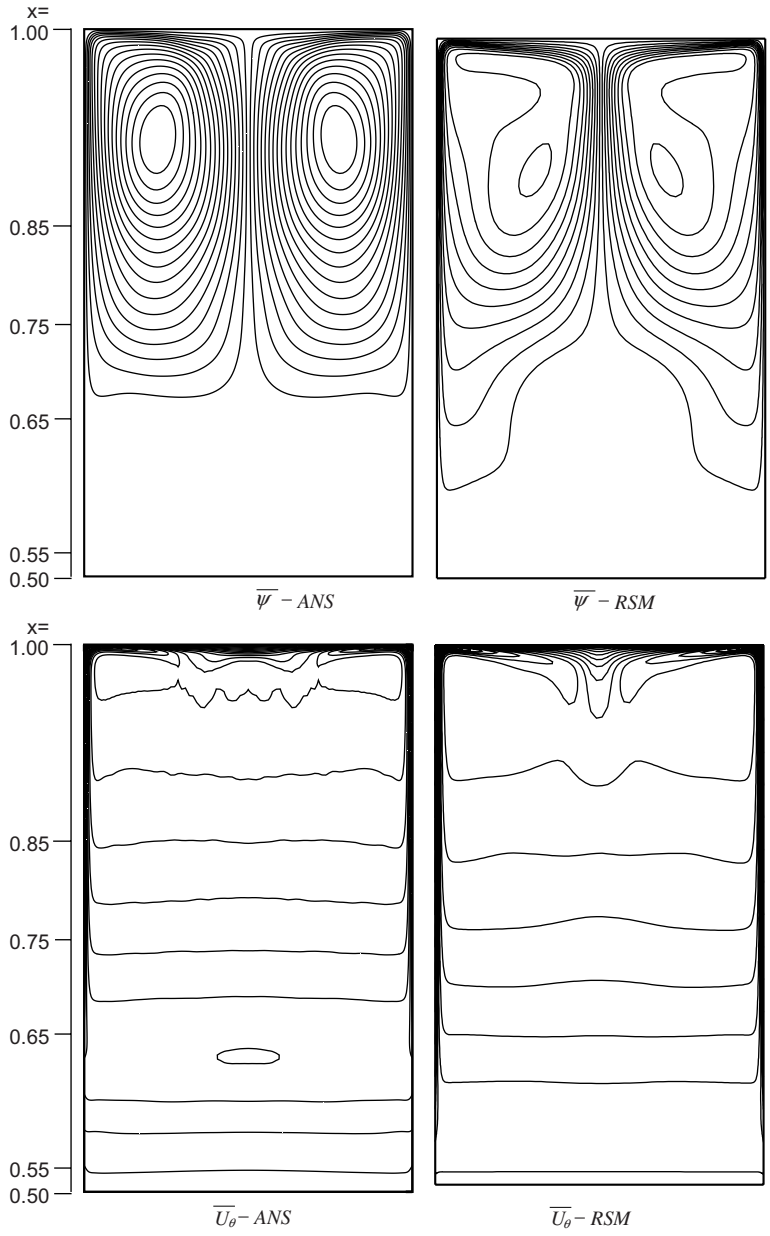

Fig. 2. Mean flow field $\overline{\psi}$ and time-averaged tangential velocity isovalues $\overline{U_\theta}$ from the axisymmetric numerical simulation (ANS) and the RSM.

particular near the two disks. Ekman-type layers clearly develop along the rotating disks in this region, but not in the inner region, and this behaviour is reflected by the tangential velocity contours. In the separation zone III (between the inner region and the core region II), the tangential velocity $\overline{U_\theta}$ exhibits a local extremum in the ANS; $\overline{U_\theta}$ shows a linear radial variation in the inner region and a $1/r$-dependence in the outer region, as indicated by the spacing between the isovalues. In the case of the RSM, the transition region III is located very close to the bottom wall (the hub), in accordance with the streamline patterns.

Gan et al. (1996) identified Rankine vortex behaviour in their measurements for this configuration. Owen and Rogers (1995) described the occurrence of such behaviour in some rotating cavity flows, characterized by the following variation of the normalized tangential velocity $U_\theta/\Omega r$ with $x^{-2} = (r/b)^{-2}$:

$$U_\theta/\Omega r = Ax^{-2} + B \tag{5.2}$$

where A and B are constants.

The variation of the time-averaged $\overline{U_\theta}/\Omega r$ with x^{-2} is shown in Fig. 3. Also reported is a steady flow solution previously obtained by Gan et al. (1996) with a first order closure based on the Launder and Sharma (1974) turbulence model (LSM). These profiles show some of the characteristics of the different regions of the flow illustrated in Fig. 2. The discrepancy in the variation of

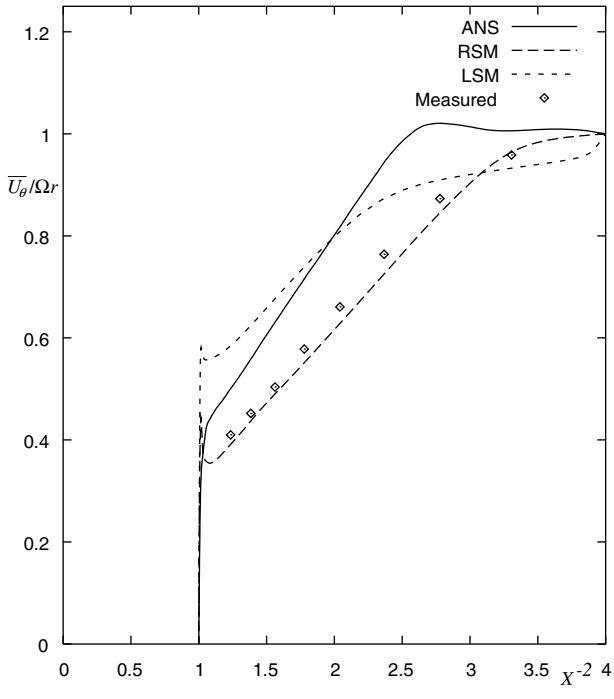

Fig. 3. Variation of the normalized tangential velocity $\overline{U_\theta}/\Omega r$ as a function of $x^{-2} = (r/b)^{-2}$ at $z/s = 0.8$.

slopes between the results in the Rankine vortex region II is due to the different behaviour of the Ekman-type boundary layers along the rotating disks obtained for the different computational approaches. In particular, due to the regularization introduced in the simulation (Eq. (3.6)), the peak observed in the other computations near $x = 1$ is replaced by a smooth variation close to the stationary casing.

Fig. 3 shows that the RSM profile follows closely the experimental data. The ANS numerical simulation, and the LSM (Gan et al., 1996), exhibit a larger extent of the inner region, characterized by near solid-body rotation satisfying the Taylor–Proudman theorem. From their experimental study for the same configuration but with $G = 0.1$, Abrahamson et al. (1989) reported the presence of solid-body rotation in the inner region extending from the hub to a radial location of about $x = 0.65$ ($x^{-2} \approx 2.37$) at a high rotation rate corresponding to $Re \approx 5 \times 10^5$. They found also that the most turbulent flow is confined within the boundary layer along the outer casing, corresponding to the only region where significant mean three-dimensional motion develops. The slight overestimate of the rotation rate ($\overline{U_\theta}/\Omega r > 1$) for the ANS to the data in the inner region (Fig. 3) compared with the measurements results from the instantaneous occurrence of small vortices with opposite circulation to the primary ones in region II, as observed by Abrahamson et al. (1989). These structures generate forced vortex behaviour (with $A = 0$ in Eq. 5.2). Such an inner region is not clearly distinguishable from the experimental data, however, nor from the RSM results. It has been already noticed that the flow rotates faster than the disks for $x^{-2} > 2.5$ for the ANS. This feature can be explained by considering the counter-rotating mean vortices in a cross section (see $\overline{\psi}$ in Fig. 2). The centrifugal flow near the disks is progressively gaining swirl, this fluid is then deflected towards the outer casing and feeds the centripetal central jet. This rapidly rotating fluid reaches regions at a lower radius where the disk velocity is weaker.

The axial variations of the normalized mean radial velocity $\overline{U_r}/\Omega r$ and tangential velocity $\overline{U_\theta}/\Omega r$ are compared with measured data at the four radial locations $x = r/b = 0.55$, 0.65, 0.75 and 0.85 (see Fig. 2) in Figs. 4–7 respectively. The profiles reflect the behaviour seen in Fig. 3. The axial mean flow profiles from the numerical simulation show symmetry with respect to the inter-disk midplane $y = z/s = 0.5$. At the innermost location, $x = 0.55$ (Fig. 4) belonging to region IV, where near solid-body rotation is expected, the profile from the numerical simulation confirms the slight overestimate of $\overline{U_\theta}$ mentioned above (see Fig. 3). From the variation of the radial velocity, we note the appearance of inward flow along the disks, with an adjacent weak outflow characterizing the presence of small vortices in these zones. According to the variation of the tangential

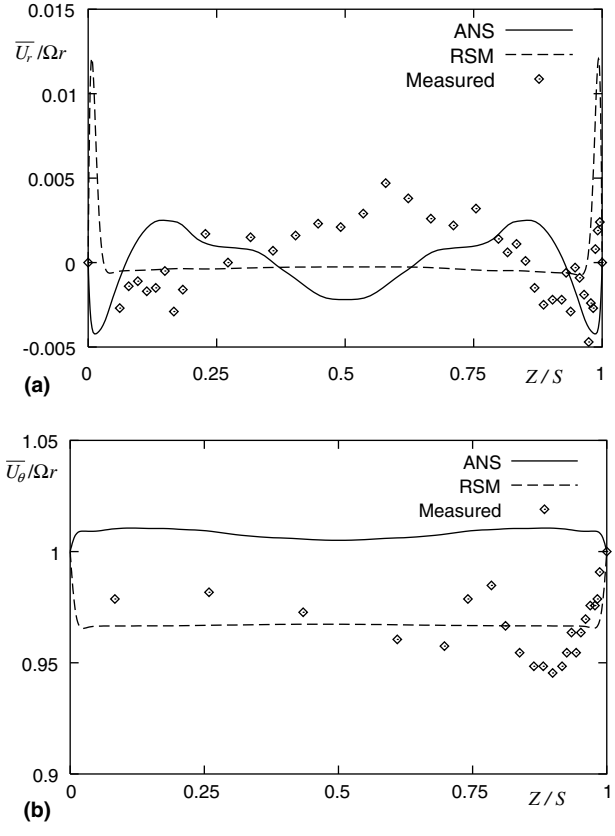

Fig. 4. Computed and measured axial variation of (a) the radial velocity $\overline{U_r}/\Omega r$ and (b) the tangential velocity $\overline{U_\theta}/\Omega r$ at $x = r/b = 0.55$.

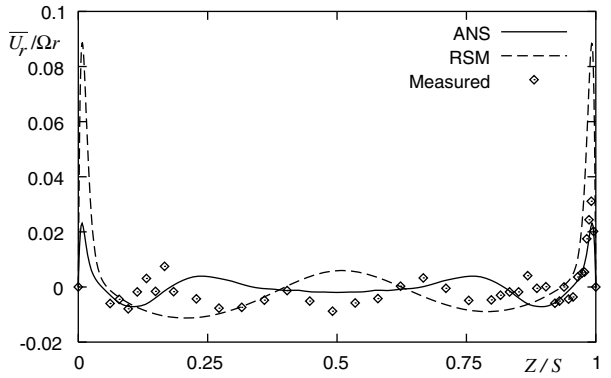

Fig. 5. Computed and measured axial variation of the radial velocity $\overline{U_r}/\Omega r$ at $x = r/b = 0.65$.

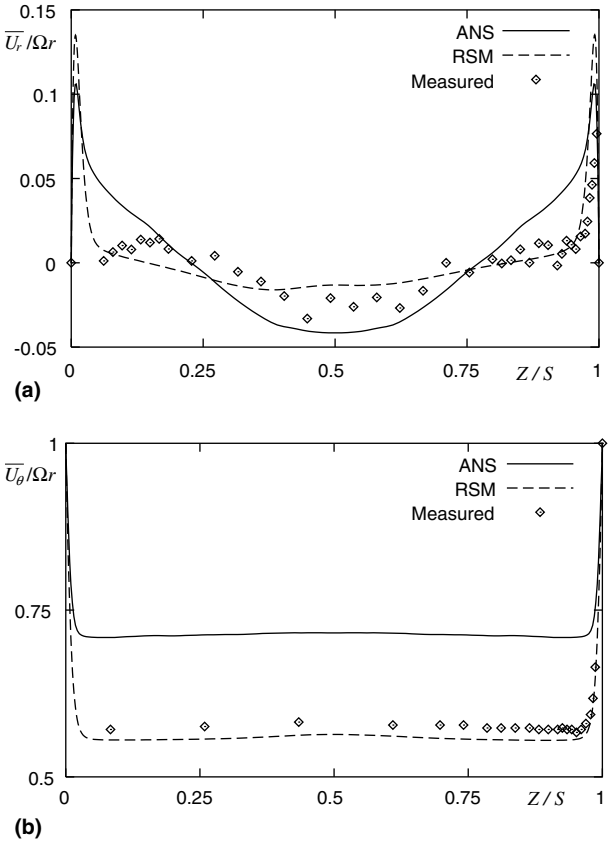

Fig. 6. Computed and measured axial variation of (a) the radial velocity $\overline{U_r}/\Omega r$ and (b) the tangential velocity $\overline{U_\theta}/\Omega r$ at $x = r/b = 0.75$.

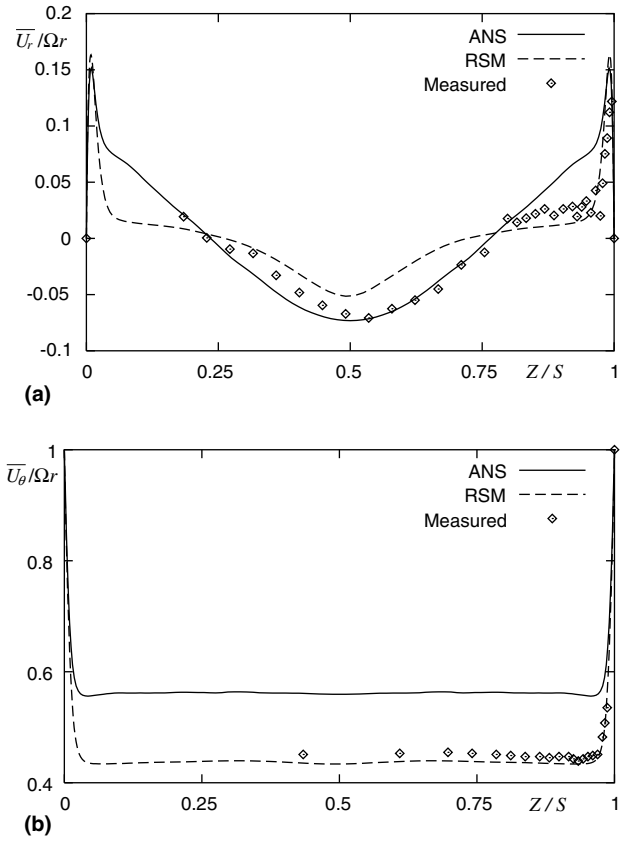

Fig. 7. Computed and measured axial variation of (a) the radial velocity $\overline{U_r}/\Omega r$ and (b) the tangential velocity $\overline{U_\theta}/\Omega r$ at $x = r/b = 0.85$.

velocity in the simulation, the disks rotate slower than the fluid thus generating inward flow on the disks. Such behaviour occurs for a fluid rotating over a stationary disk (see Bödewadt, 1940; Schlichting, 1968). The measured radial velocities are very small and do not support conclusively either radial inflow on the disks, or the outflow in very thin boundary layers obtained for the RSM solution. Both the measured tangential velocity and the RSM solution suggest slower rotation of the flow compared to the disks, so that this location $x = 0.55$ already corresponds to region II (with $x^{-2} = 3.306$ in Fig. 3) for the RSM results and the experiments.

The location $x = 0.65$ is in the region of the detached shear layer (region III in Fig. 2), known to act like a compliant surface between regions II and IV. (Experimental data are available for the radial velocity only at this location.) The development of the Ekman-type layers on the disks is evident in both the ANS simulation and the measurements, while these boundary layers are well established in the RSM results (Fig. 5). Depending on the radius location x, there is also different behaviour between the boundary layers, but in each case the levels of radial velocity are very small. Fig. 3 shows that there are significant differences in the behaviour of the mean tangential velocity at the midplane for the different sets of results around this location $x = 0.65$ (corresponding to $x^{-2} = 2.37$).

At radial locations closer to the stationary outer casing (Figs. 6 and 7), the Ekman-type layers are very thin, with outflow just outside the boundary layers suggested by the experimental data. The measured radial velocity variation at both radial locations is reasonably well represented by the RSM results. The ANS gives

only qualitative agreement in comparison with the measurements, particularly in the region of the central inflow around $z/s = 0.5$. The peak radial velocity in the boundary layer at $x = 0.85$ (corresponding to the region II) is similar for both computations. All of the results show virtually uniform tangential velocity between the boundary layers, with the ANS simulation giving too high a rotation rate (as also shown in Fig. 3 with $x^{-2} < 1.78$ for $x > 0.75$). The deficiencies of the ANS are visible for both the radial and the tangential velocity components, and this is explained by the axisymmetry assumption: the coherent vortices observed in the near-wall region for a real turbulent boundary layer cannot be present in the flow field resulting from the ANS.

The total kinetic energy $\widehat{k} = 0.5\widehat{R_{jj}}$ (see Eq. (5.1)) is reported in Fig. 8 for the numerical simulation and the RSM. These include both macrocomponents and turbulent contributions. There is qualitative correspondence between the two approaches, but, differences appear towards the inner region where low levels of turbulence develop, resulting from the motion of small vortices in this region as already displayed by the velocity profiles. High turbulence values now occur in the boundary layers, and the boundary layer transition to turbulence is located approximately at the mid-height of the cavity. The RSM result clearly shows the turbulent energy in the thin Ekman layers. A sharp peak in turbulence develops at the upper corners. This is less pronounced in the ANS result because of the numerical smoothing (Eq. (3.6)) introduced at the corners. The highest turbulence levels in the RMS are found in the strongly sheared layers on the stationary casing formed from the outward flow on the disks. Turbulence is then convected into the jet where the levels decrease.

The ANS contours shown in Fig. 8 reveal that practically no turbulence is produced in the Ekman layers along the rotating disks, in contrast with the real DNS by Coleman et al. (1990) and Lygren and Andersson (2001). Nevertheless, the ANS results compare fairly well with the experimental data and the RSM predictions, suggesting some justification for the ANS.

The comparisons presented in Figs. 3–7 show that the unsteady RSM predictions are in closer overall agreement with the measurements than the ANS predictions. The RSM calculations imply only axisymmetry of the mean quantities, and full account is taken of the Reynolds stress components. The ANS allows a more detailed calculation of the instantaneous flow characteristics but the axisymmetry hypothesis is applied over the whole velocity field, impeding the development of truly three-dimensional turbulence.

5.2. Unsteady flow

In order to investigate the periodic nature of the flapping jet between the two disks, induced by organized macrocomponents $\widetilde{u}_i$, we have considered the local mass flowrate circulating within the cavity. The temporal evolution of the instantaneous dimensionless flowrate computed through the half cross-section $0 \leqslant y =$

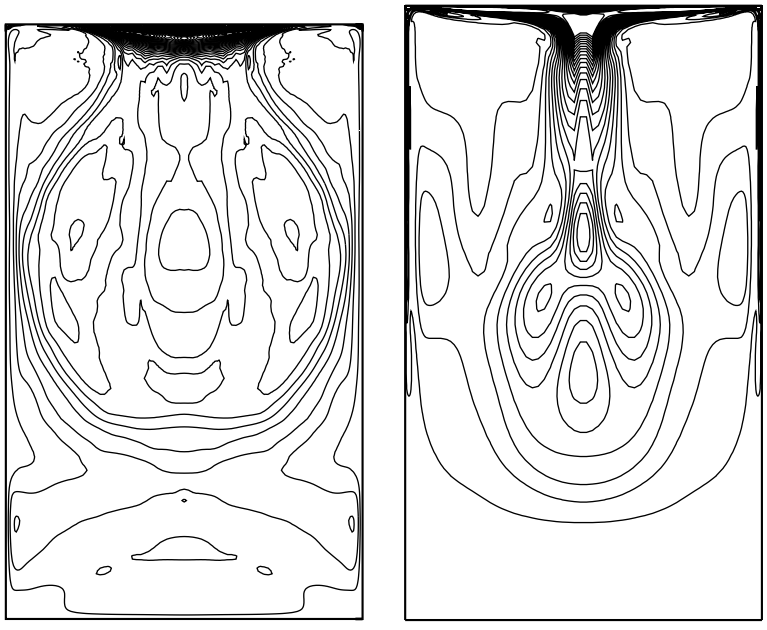

ANS RSM

Fig. 8. Isocontour plots of the total kinetic energy: for the ANS, 33 levels with $0 \leqslant \widehat{k}/(\Omega^2 s^2) \leqslant 0.11312$, and for the RSM, $0 \leqslant \widehat{k}/(\Omega^2 s^2) \leqslant 0.0765$ with an increment of 0.0003.

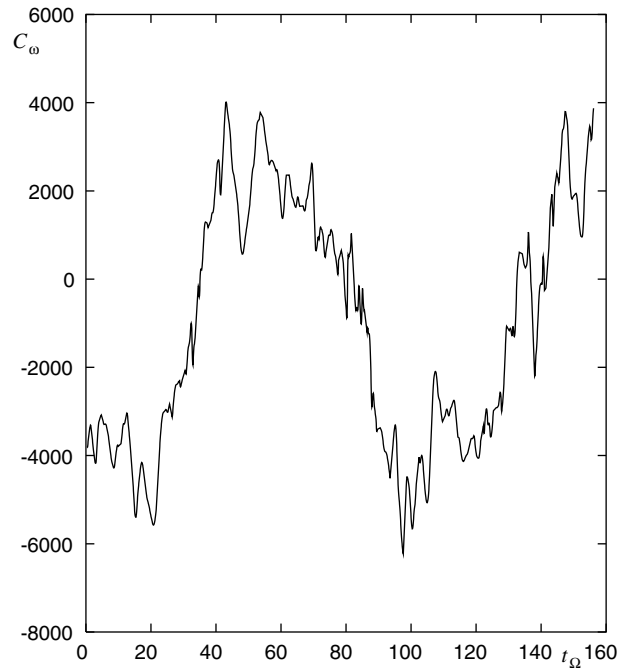

Fig. 9. Temporal evolution of the instantaneous local flowrate between $y = z/s = 0$ and $y = 0.5$ at $x = r/b = 0.92$: ANS.

$z/s \leqslant 0.5$ is shown in Fig. 9 at a fixed value of the radial location x. The local mass flow is defined as

$$\dot{m} = 2\pi\rho r \int_0^{s/2} U_r \, \mathrm{d}z$$

giving in dimensionless form:

$$C_w = \frac{\dot{m}}{\mu b} = \pi x Re \int_0^{0.5} U_r \, \mathrm{d}z$$

where x is the radial location at which the flowrate is computed. We have taken a value $x = 0.92$ before the "jet" impinges upon the disk (similar to the Coanda effect, Tritton, 1988).

We can identify a period $T\Omega = 104$ from Fig. 9, while in the present results the RSM was found to produce a periodic behaviour with $T\Omega \approx 86$.

The temporal evolution of the instantaneous kinetic energy $k = \langle u_i' u_i' \rangle / 2$ over half a period $T\Omega/2$ is displayed in Fig. 10 from the ANS and in Fig. 11 from the RSM. The contours from the ANS correspond to fixed isovalues of the kinetic energy.

From the ANS results, it is worthwhile to note first the time spent by the "jet" along the central line, which is relatively short compared with the evolution towards the disks. Unsteadiness is induced specifically by the central jet, while the lateral boundary layers exhibit almost steady behaviour. The unsteady behaviour is only apparent on the U_r and U_z velocity components in the central region of the cavity where the jet develops. Fig. 3, representing time mean values $\overline{U_\theta}$, would not be significantly different if instantaneous $\langle U_\theta \rangle$ values were used. The flapping motion is also associated with a shift of the location along the stationary casing where the jet originates; this is not clearly distinguishable from the RSM results, indeed the turbulence levels within the jet decrease towards the centre of the cavity. Reverse flow can be observed from the contours of the instantaneous kinetic energy obtained with both the ANS and RSM. Similarity with an impinging jet in a cavity can be observed, with a feedback effect (see Mataoui et al., 2003). However, the main difference comes from the moving of the jet origin on the outer casing. In the present configuration the feedback is generated by the separation region III, seen to be limited to around $x = 0.6$. Small vortices develop within the inner region, but remain in this region, even though exchange between regions II and IV does occur (Randriamampianina et al., 2001). The residual wiggles, appearing in the upper part of the cavity (see Fig. 10), correspond to very weak values and probably result from the boundary conditions at the upper corners, where very strong shear stresses develop at the junction between the rotating disks and the stationary casing. We recall that these isocontours have been taken at the same values to follow their temporal behaviour, corresponding to small values of the vorticity. On the other hand, Botella and Peyret (1998) have proposed a subtraction technique to remove effects (recalling the Gibbs phenomena) resulting from singularities at corners, as in the case of the classical lid-driven cavity. Such a filtering approach could be introduced in the present computations, but the observed wiggles do not significantly affect the flow behaviour.

Fig. 11 illustrates the flow patterns during half a period of time from the RSM. These are in qualitative agreement with the ANS results shown in Fig. 10, and exhibit clearly the alternate deviation of the centripetal jet between the two disks. In each case, the jet pattern passing through the centre line is very short-lived. Most of the time, the jet is deflected towards one or other of the disks.

6. Discussion

A crude physical model of the mechanisms involved is proposed. If the transverse velocity is supposed to be mainly governed by pressure effects, then the z-component of the momentum equation reduces to

$$\frac{\mathrm{d}U_z}{\mathrm{d}t} \approx -\frac{\partial(P + \rho\overline{u_z'^2})}{\partial z} \tag{6.1}$$

If η denotes the shift of the jet axis from the symmetry line due to the deflection of the jet at the mean location of the impingement h, then

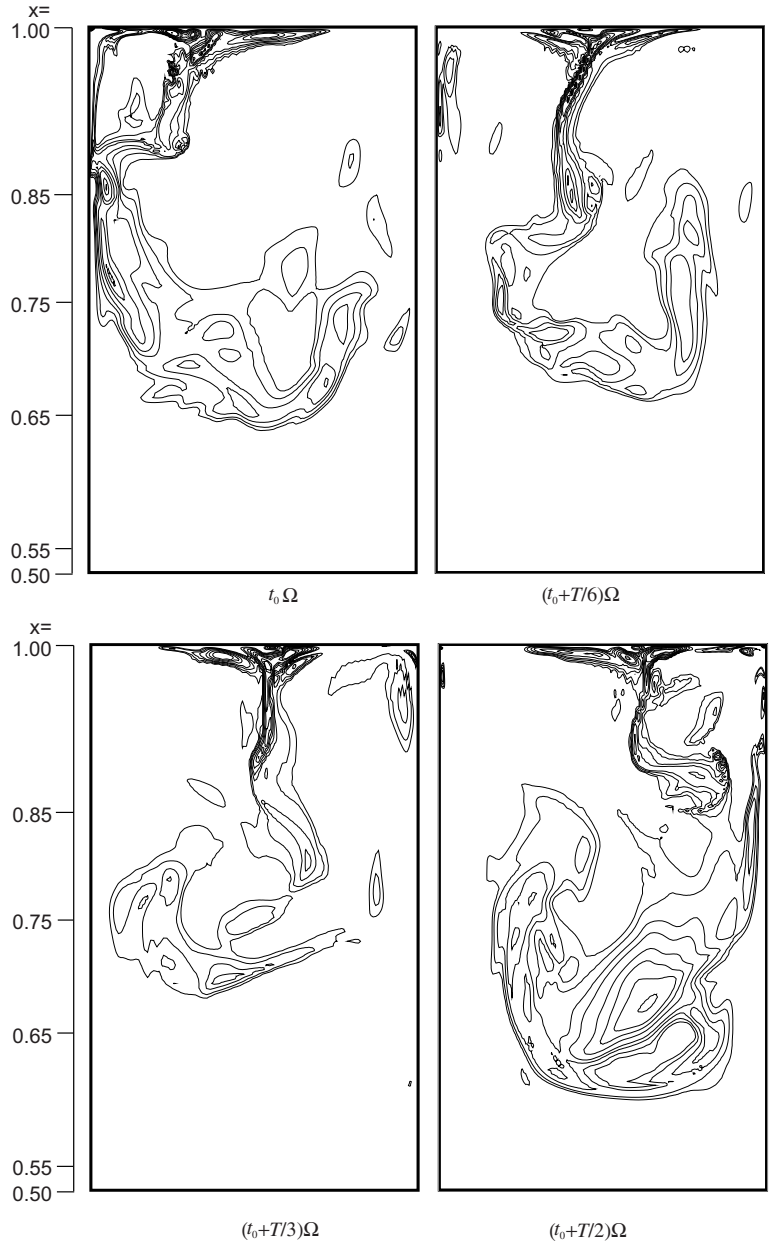

Fig. 10. Temporal evolution of the instantaneous kinetic energy $k = \langle u_i' u_i' \rangle / 2$ during half a period $T\Omega/2$: ANS, 10 levels with $0.001 \leqslant k/(\Omega^2 s^2) \leqslant 0.0325$.

$$\frac{\mathrm{d}\eta}{\mathrm{d}t} = U_z \quad \text{and} \quad \frac{\mathrm{d}^2\eta}{\mathrm{d}t^2} \approx -\frac{\partial(P + \rho\overline{u_z'^2})}{\partial z} \tag{6.2}$$

Assuming now that the pressure is created by the kinetic energy of the normal component at the jet impingement:

$$P = \frac{(U_J \sin\alpha)^2}{2} \quad \text{and} \quad \frac{\partial(P + \rho\overline{u_z'^2})}{\partial z} = \frac{U_J^2 \mid \eta \mid \eta}{2h^2 s} \tag{6.3}$$

where α is the angle of deflection of the jet, such that $\sin\alpha = U_z/U_J$, where U_J is the velocity on the jet axis. These velocities can be considered as phase averages.

If $|\eta|$ is approximated by its mean value $s/4$, this gives

$$\frac{\partial(P + \rho\overline{u_z'^2})}{\partial z} = \frac{U_J^2}{8h^2}\eta$$

and finally the equation of motion for the flapping of the jet

$$\frac{\mathrm{d}^2\eta}{\mathrm{d}t^2} = -\frac{U_J^2}{8h^2}\eta$$

allows the frequency of the oscillation to be determined:

$$f = \frac{\omega}{2\pi} = \frac{1}{2\pi}\frac{U_J}{h\sqrt{8}} \tag{6.4}$$

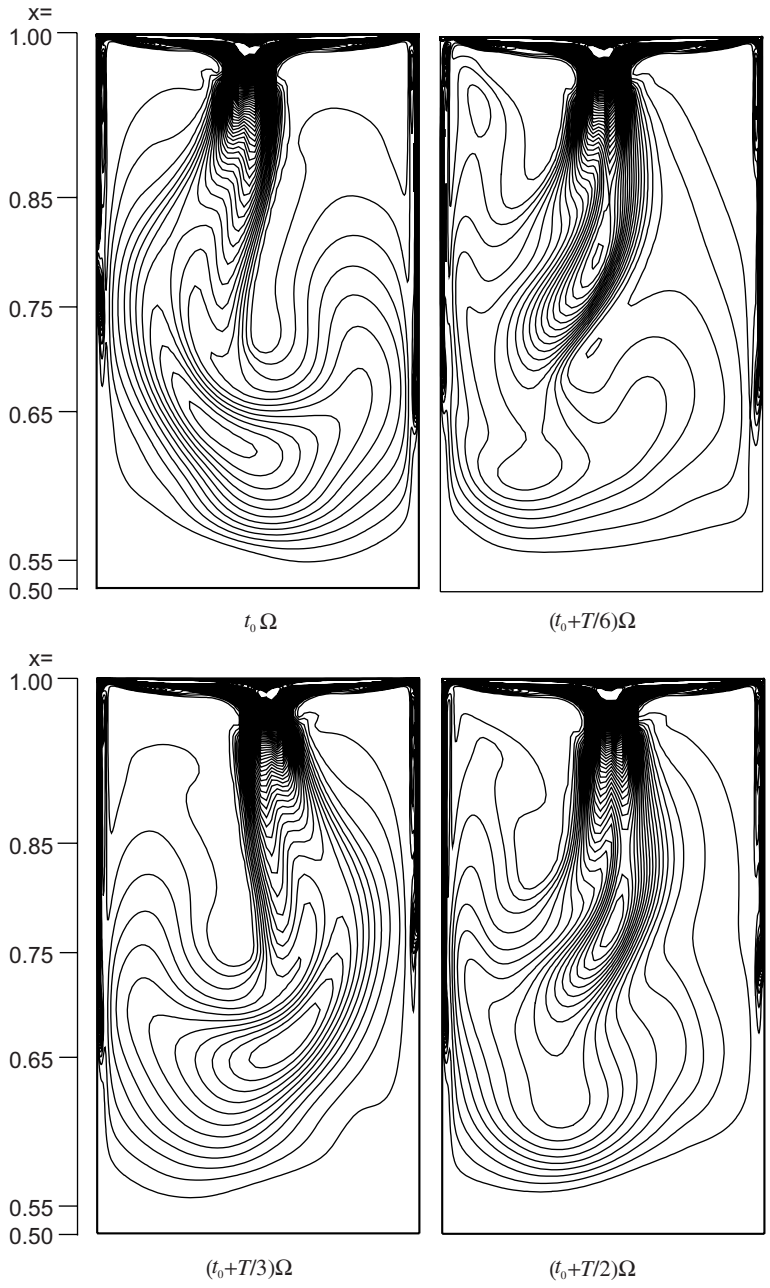

Fig. 11. Temporal evolution of the kinetic energy $k = \langle u_i' u_i' \rangle / 2$ during half a period $T\Omega/2$: RSM, $0 \leqslant k/(\Omega^2 s^2) \leqslant 0.0765$ with an increment of 0.0003.

Considering that the two Ekman layers along the disks are the source of the recirculating flow feeding the central jet, this recirculating mass flowrate can be considered constant. The mean velocity on the jet axis near the point of impingement r_J on the disks is denoted by U_J. Assuming that the mass flowrate is

$$\frac{\dot{m}}{\mu r_J} = \frac{2\pi U_J \Delta_{\max}}{\nu}$$

we thus have

$$\frac{2\pi U_J \Delta_{\max}}{\nu} = \frac{C_{w\max}}{x_J}, \quad x_J = \frac{r_J}{b}$$

and finally

$$f = \frac{1}{4\pi^2\sqrt{8}} \frac{\nu}{h\Delta_{\max}} \frac{C_{w\max}}{x_J} = \frac{1}{4\pi^2\sqrt{8}} \frac{C_{w\max}}{x_J Re} \frac{b^2}{h\Delta_{\max}} \Omega$$

or

$$T\Omega = 4\sqrt{8}\pi^2 \frac{h\Delta_{\max}}{b^2} \frac{x_J Re}{C_{w\max}}$$

For the present configuration, with $Re = 1.46 \times 10^5$ and $s/b = 0.3$, and taking the value $C_{w\max} = 4000$ from Fig. 9 this corresponds to

$$T\Omega \approx 85.6$$

where the mean value of the radial location of the jet is given by $x_J \approx 0.7$ i.e. midway between the observed limits of the jet impingement $x = 0.9$ and $x = 0.5$ (see Fig. 10), so that $h/b = 1 - x_J = 0.3$. The mean value of the jet width can be estimated in this expression by $\Delta_{\max} \approx s/3$ on the basis of the present numerical results.

Thus, from these relations we can deduce a Reynolds number for the jet:

$$R(x_J) = \frac{U_J \Delta_{\max}}{\nu} = \frac{C_{w\max}}{2\pi x_J} \approx 909.5$$

We note the good agreement for the prediction of the period of jet oscillations between the theoretical value and the result obtained from the RSM computations. The very close agreement observed between the available experimental data and the results from the RSM suggests that the period of the jet oscillation in the present configuration with the parameters considered is $T\Omega \approx 86$.

7. Concluding remarks

The turbulent flow in an enclosed corotating disk pair with a stationary outer casing has been investigated numerically for a rotational Reynolds number $Re = 1.46 \times 10^5$, corresponding to the experimental study of Gan et al. (1996). An axisymmetric numerical simulation and one point statistical modelling of the flow have been performed. Both approaches produce an unsteady periodic behaviour for the mean flow. This is visible mainly for the central recirculating flow, which takes on the appearance of a flapping centripetal jet originating from the boundary layers developing along the stationary outer casing. The Ekman layers along the rotating disks are found to be almost steady. A high level of turbulence intensity is reached in the region near the upper corners of the cavity, where strong shear is generated between the periphery of the rotating disks and the stationary casing. On the other hand, very weak intensities of turbulence prevail towards the innermost region of the cavity, where a low speed fluid layer behaves like a cushion at which the central jet is deflected.

The overall structure of the mean flow is consistent with the five regions described by Schuler et al. (1990), and comparisons with experimental data show reasonable agreement. In particular, the mean tangential velocity variation along the radial direction confirms the Rankine vortex behaviour found by Gan et al. (1996). There is very good agreement between experimental measurements and RSM predictions. The unsteady nature of the flow produced by the flapping jet explains the main features of the isocontour plots of turbulence double velocity correlations. The frequency of the oscillating motion is relatively low compared with the rotational frequency of the disks. A simplified analytical model suggests that the driving force for the unsteadiness is linked to pressure–velocity effects rather than instabilities convected from the Ekman layers. It is remarkable that the one point statistical closure succeeds in representing this unsteady behaviour. The present results confirm that RSM modelling may be an attractive means to compute turbulent confined flows in the presence of rotation, and to recover some unsteady features of the flows.

The unsteady RSM predictions, due to a full account of the individual stress components, are in closer agreement with the experimental data than the ANS predicitions. In spite of the axisymmetry hypothesis, the ANS numerical simulation produced a detailed description of the instantaneous flow structures and turbulence correlations (obtained by statistical treatment) that are compatible with both the experimental data and the RSM predictions. Despite the fact that the axisymmetry assumption precludes some purely three-dimensional features such as vortex stretching, some redistribution mechanisms are included which lead to results with noticeably different behaviour to those observed in purely two-component planar flows. Full three-dimensional simulations will be carried out in the future in order to account for the three-dimensional mechanisms of actual turbulence.

Acknowledgements

These computations have been performed on the NEC SX-5 and T3E of the IDRIS (CNRS, Orsay, France). AR would like to acknowledge the valuable discussions with Pr. J. M. Owen (University of Bath, UK) and Pr. E. Villermaux (IRPHE, Marseille). The authors are grateful to the CNRS and the Royal Society for their financial support.

Appendix A. Model equations in a nonrotating frame of reference

The transport equations of the turbulent stresses (see Section 4.1)

$$\frac{\mathrm{d}R_{ij}}{\mathrm{d}t} = P_{ij} + D_{ij}^{\mathrm{T}} + \underbrace{\phi_{ij}^{(1)} + \phi_{ij}^{(2)} + \phi_{ij}^{(R)} + \phi_{ij}^{(W)}}_{\Phi_{ij}} - \varepsilon_{ij} + \nu R_{ij,ss} + \underbrace{D_{ij}^{R} + B_{ij} + J_{ij}}_{\text{extra terms}(R)} \tag{A.1}$$

are detailed by specifying each term in the right-hand side:

Production term of the Reynolds stresses

$$P_{ij} = -R_{im}U_{j,m} - R_{jm}U_{i,m} \tag{A.2}$$

Production of turbulent kinetic energy

$$P = \frac{1}{2}P_{jj}$$

Turbulent diffusion

$$D_{ij}^{\mathrm{T}} = C_S(\sigma_{pm}R_{ij,p})_{,m} \tag{A.3}$$

with

$$\sigma_{pm} = \frac{k \cdot R_{pm}}{\varepsilon}$$

Pressure–strain correlation: nonlinear part

$$\phi_{ij}^{(1)} = -\left[\tilde{c}_1 a_{ij} + c_1'(a_{ip}a_{pj} - \frac{1}{3}A_2\delta_{ij})\right]\varepsilon \tag{A.4}$$

with

$$\tilde{c}_1 = (3.1\sqrt{A \cdot A_2} + 1) \cdot [1 - \exp(-Re_T^2/40)]$$

$$c_1' = 3.72\sqrt{A \cdot A_2} \cdot [1 - \exp(-Re_T^2/40)]$$

Pressure–strain correlation: linear part

$$\begin{aligned}\phi_{ij}^{(2)} = {} & -0.6\left(P_{ij} - \frac{1}{3}P_{ss}\delta_{ij}\right) + 0.3\varepsilon.a_{ij}\frac{P_{ss}}{\varepsilon} \\ & - 0.2\left\{\frac{R_{mj}R_{li}}{k}(U_{m,l} + U_{l,m}) - \frac{R_{lm}}{k}(R_{im}U_{j,l}\right. \\ & \left. + R_{jm}U_{i,l})\right\} - \min(0.6, A) \cdot \left[A_2(P_{ij} - D_{ij})\right. \\ & \left. + 3a_{mi}a_{nj}(P_{mn} - D_{mn})\right]\end{aligned} \tag{A.5}$$

Pressure–strain correlation: wall reflection term with rotation effect

$$\begin{aligned}\phi_{ij}^{(w)} = {} & c_2'\left[(\phi_{pm}^{(2)} + \phi_{pm}^{(R)})n_p n_m \delta_{ij} - \frac{3}{2}(\phi_{ip}^{(2)} + \phi_{ip}^{(R)})n_p n_j\right. \\ & \left. - \frac{3}{2}(\phi_{pj}^{(2)} + \phi_{pj}^{(R)})n_p n_i\right]\frac{k\sqrt{R_{pq}n_p n_q}}{\varepsilon y}\end{aligned} \tag{A.6}$$

where y is the distance from the nearest wall and n_p is the normal unit vector at the wall.

Dissipation rate of the Reynolds stresses

$$\varepsilon_{ij} = f_A\varepsilon_{ij}^* + (1 - f_A)\left[f_S\frac{\varepsilon R_{ij}}{k} + \frac{2}{3}(1 - f_S)\varepsilon \cdot \delta_{ij}\right] \tag{A.7}$$

$$f_A = \exp(-20A^2) \cdot \exp(-Re_T^2/20)$$

$$f_S = \exp(-Re_T^2/40)$$

$$\text{with } Re_T = \frac{k^2}{\nu\tilde{\varepsilon}}$$

Limiting wall values of the dissipation rates

$$\varepsilon_{ij}^* = \frac{\varepsilon}{k} \cdot \frac{R_{ij} + R_{im}n_j n_m + R_{jm}n_i n_m + R_{ml}n_l n_m n_i n_j}{1 + \frac{3}{2}\frac{R_{pq}}{k}n_p n_q}$$

Dissipation rate of turbulent kinetic energy equation

$$\begin{aligned}\frac{\mathrm{d}\varepsilon}{\mathrm{d}t} = {} & -C_{\varepsilon 1}\frac{\varepsilon}{k}R_{ij}U_{i,j} - C_{\varepsilon 2}f_\varepsilon\frac{\tilde{\varepsilon} \cdot \varepsilon}{k} + \left(C_\varepsilon\frac{k \cdot R_{ij}}{\varepsilon}\varepsilon_{,j} + \nu\varepsilon_{,i}\right)_{,i} \\ & + C_{\varepsilon 3}\nu\frac{k}{\varepsilon}R_{jm}U_{i,jl}U_{i,ml} + C_{\varepsilon 4}\left(\nu\frac{\tilde{\varepsilon}}{k}k_{,i}\right)_{,i}\end{aligned} \tag{A.8}$$

with

$$f_\varepsilon = 1/(1 + 0.63\sqrt{A \cdot A_2})$$

Extra terms due to rotation effects (see Schiestel and Elena, 1997):

- Extra term in the pressure–strain contribution

$$\phi_{ij}^{(R)} = -0.6\left(D_{Cij} - \frac{2}{3}P_C\delta_{ij}\right) - \frac{2}{5}k(U_{i,j} + U_{j,i}) \tag{A.9}$$

$$P_{Cij} = -C_{ip}U_{j,p} - C_{jp}U_{i,p}, \quad D_{Cij} = -C_{ip}U_{p,j} - C_{jp}U_{p,i}$$

$$P_C = \frac{1}{2}P_{Cmm} = \frac{1}{2}D_{Cmm} = -C_{ip}U_{i,p}$$

- Inhomogeneous effects

$$D_{ij}^R = C_S\left(\frac{k^2}{\varepsilon}f_{Ro}Y_{lm}R_{ij,l}\right)_{,m} \tag{A.10}$$

$$f_{Ro} = \frac{2.Ro_t^{-1/2}}{1 + 15.Ro_t^{-1/2}}, \quad Y_{lm} = \frac{\Omega_l^*\Omega_m^*}{\Omega^{*2}}$$

where Ω_i^* denotes the intrinsic rotation vector.

- Spectral jamming term

$$B_{ij} = -\alpha_B\left(R_{ij} - k \cdot \delta_{ij} + \frac{1}{2}C_{ij}\right) \tag{A.11}$$

with the structure parameter:

$$C_{ij} = \frac{2}{3}\left(1 + \frac{f_C}{2}\right)k \cdot \delta_{ij} - f_C \cdot k\frac{\Omega_i^*\Omega_j^*}{\Omega^{*2}}$$

and

$$\alpha_B = \frac{1}{2}\Omega^*\frac{C_{pq}Y_{pq}}{2k}, \quad f_C = \frac{Ro_t^{-1}}{5 + Ro_t^{-1}}$$

- Inverse flux due to rotation which opposes the energy cascade

$$J_{ij} = \frac{2}{3}\left[(1 - f_T)\delta_{ij} + f_T\frac{R_{ij}}{2k/3}\right]J \tag{A.12}$$

$$J = \frac{f_J}{1 + f_J}\tilde{\varepsilon}, \quad f_T = \frac{1}{1 + Re_t/10}$$

$$f_J = \frac{0.12\,Ro_t^{-2} + 0.015\,Ro_t^{-1} - 0.3\exp(-Re_t^2)\cdot(0.4\,Ro_t^{-2} + 0.05\,Ro_t^{-1})}{0.254\,Ro_t^{-2} + 0.1567\,Ro_t^{-1} + 1}$$

$$Ro_t = \frac{\varepsilon}{k\cdot\Omega^*}, \quad A = 1 - \frac{9}{8}(A_2 - A_3), \quad A_2 = a_{ij}a_{ij}, \quad A_3 = a_{ij}a_{jk}a_{ki}$$

Numerical coefficients:

$$C_2' = 0.2, \quad C_S = 0.22, \quad C_\varepsilon = 0.18, \quad C_{\varepsilon 1} = 1.0, \quad C_{\varepsilon 2} = 1.92, \quad C_{\varepsilon 3} = 2.0, \quad C_{\varepsilon 4} = 0.92$$

References

Abrahamson, S.D., Eaton, J.K., Koga, D.J., 1989. The flow between shrouded corotating disks. Phys. Fluids A 1, 241–251.

Akhmetov, D.G., Tarasov, V.F., 1987. Structure and evolution of vortex cores. J. Appl. Mech. Tech. Phys. 27, 690–694.

Bödewadt, U.T., 1940. Die Drehströmung über festem Grunde. Z. Angew. Math. Mech. 20, 241.

Botella, O., Peyret, R., 1998. Benchmark spectral results on the lid-driven cavity flow. Comput. Fluids 27, 421–433.

Cambon, C., Jacquin, L., 1989. Spectral approach to non-isotropic turbulence subjected to rotation. J. Fluid Mech. 202, 295–317.

Cambon, C., Jacquin, L., Lubrano, J.L., 1992. Towards a new Reynolds stress model for rotating turbulent flow. Phys. Fluids A 4, 812–824.

Canuto, C., Hussaini, M.Y., Quarteroni, A., Zang, T.A., 1987. Spectral Methods in Fluid Dynamics. Springer Verlag.

Chaouche, A.M., Randriamampianina, A., Bontoux, P., 1990. A collocation method based on an influence matrix technique for axisymmetric flows in an annulus. Comput. Methods Appl. Mech. Eng. 80, 237–244.

Chasnov, J.R., 1995. The decay of axisymmetric homogeneous turbulence. Phys. Fluids A 7 (3), 600–605.

Coleman, G.N., Ferziger, J.H., Spalart, P.R., 1990. A numerical study of the turbulent Ekman layer. J. Fluid Mech. 213, 313–348.

Crespo del Arco, E., Maubert, P., Randriamampianina, A., Bontoux, P., 1996. Spatio-temporal behaviour in a rotating annulus with a source-sink flow. J. Fluid Mech. 328, 271–296.

Daly, B.J., Harlow, F.H., 1970. Transport equation of turbulence. Phys. Fluids A 13, 2634.

Elena, L., 1994. Modélisation de la turbulence inhomogène en présence de rotation. Thèse de Doctorat, Univ. Aix-Marseille II, France.

Elena, L., Schiestel, R., 1995a. Turbulence modeling of confined flow in rotating disc systems. AIAA Journal 33 (1), 812–821.

Elena, L., Schiestel, R., 1995b. Résolution numérique des équations de transport des tensions de Reynolds en écoulements turbulents tournants en milieu confiné. Revue Européenee des Eléments Finis 4 (1), 7–32.

Elena, L., Schiestel, R., 1995c. Turbulence modeling of rotating confined flow. Proc. Xth Int. Symp. Turbulent Shear Flows 1, 8.25.

Elena, L., Schiestel, R., 1996. Turbulence modeling of rotating confined flows. Int. J. Heat Fluid Flow 17 (3), 283–289.

Gan, X., Mirzaee, I., Owen, J.M., Rees, D.A.S., Wilson, M., 1996. Flow in a rotating cavity with a peripheral inlet and outlet of cooling air. In: ASME Int. Gas Turbine and Aeroengine Cong., paper 96-GT-309, Birmingham.

Gauthier, G., Gondret, P., Rabaud, M., 1999. Axisymmetric propagating vortices in the flow between a stationary and a rotating disk enclosed by a cylinder. J. Fluid Mech. 386, 105–126.

Gibson, M., Launder, B.E., 1978. Ground effects on pressure fluctuations in the atmospheric boundary layer. J. Fluid Mech. 86, 491.

Gottlieb, D., Orszag, S.A., 1977. Numerical analysis of spectral methods: theory and applications. CBMS Regional Conf. Series in Appl. Math., SIAM.

Haldenwang, P., Labrosse, G., Abboudi, S., Deville, M., 1984. Chebyshev 3-D spectral and 2-D pseudospectral solvers for the Helmholtz equation. J. Comput. Phys. 55, 115–128.

Herrero, J., Giralt, F., Humphrey, J.A.C., 1999. Influence of the geometry on the structure of the flow between a pair of corotating disks. Phys. Fluids 11, 88–96.

Huang, P.G., Leschziner, M.A., 1985. Stabilization of recirculating flow computations performed with second moments closures and third order discretization. In: Vth Int. Symp. on Turbulent Shear Flow, Cornell University, August 7–9.

Hugues, S., Serre, E., Crespo del Arco, E., Randriamampianina, A., Bontoux, P., 1998. Instabilité tridimensionnelle de la couche d'Ekman dans une configuration annulaire avec flux forcé. C.R. Acad. Sci. II Paris 326 (b), 873–879.

Jacques, R., Le Quéré, P., Daube, O., 2002. Axisymmetric numerical simulations of turbulent flows in rotor–stator enclosures. Int. J. Heat Fluid Flow 23 (4), 381–397.

Kassinos, S.C., Reynolds, W.C., Rogers, M.M., 2001. One-point turbulence structure tensors. J. Fluid Mech. 428, 213–248.

Launder, B.E., Reynolds, W.C., 1983. Asymptotic near-wall stress dissipation rates in a turbulent flow. Phys. Fluids A 26 (5), 1157.

Launder, B.E., Sharma, B.I., 1974. Application of the energy-dissipation model of turbulence to the calculation of flow near a spinning disk. Lett. Heat Mass Transfer 1, 131.

Launder, B.E., Tselepidakis, D.P., 1994. Application of a new second-moment closure to turbulent channel flow rotating in orthogonal mode. Int. J. Heat Fluid Flow 15 (1), 2.

Lesieur, M., 1990. Turbulence in Fluids, second ed. Kluwer, Dordrecht.

Lygren, M., Andersson, H.I., 2001. Turbulent flow between a rotating and a stationary disk. J. Fluid Mech. 426, 297–326.

Mataoui, A., Schiestel, R., Salem, A., 2003. Study of the oscillatory regime of a turbulent plane jet impinging in a rectangular cavity. Appl. Math. Modell. 27, 89–114.

Mirzaee, I., Wilson, M., Owen, J.M., 1997. Heat transfer in a rotating cavity with a peripheral inflow and outflow of cooling air. In: ASME Int. Gas Turbine and Aeroengine Cong., paper 97-GT-136, Orlando.

Owen, J.M., Rogers, R.H., 1995. Flow and heat transfer in rotating disc systems: vol. 2, Rotating cavities, Research Studies Press, Taunton, UK.

Randriamampianina, A., Bontoux, P., Roux, B., Argoul, P., 1986. Multistep methods for spectral Tau–Chebyshev approximation. Application to rotating and buoyancy driven internal flows. Notes Numer. Fluid Mech., Vieweg 13, 302–309.

Randriamampianina, A., Bontoux, P., Roux, B., 1987. Ecoulements induits par la force gravifique dans une cavité cylindrique en rotation. Int. J. Heat Mass Transfer 30 (7), 1275–1292.

Randriamampianina, A., Elena, L., Fontaine, J.P., Schiestel, R., 1997. Numerical prediction of laminar, transitional and turbulent flows in shrouded rotor–stator systems. Phys. Fluids 9 (6), 1696–1713.

Randriamampianina, A., Schiestel, R., Wilson, M., 2001. Spatio-temporal behaviour in an enclosed corotating disk pair. J. Fluid Mech. 434, 39–64.

Reynolds, W.C., Hussain, A.K.M.F., 1972. The mechanics of an organized wave in turbulent shear flow. Part 3. Theoretical models and comparisons with experiments. J. Fluid Mech. 54 (2), 263–288.

Serre, E., Hugues, S., Crespo del Arco, E., Randriamampianina, A., Bontoux, P., 2001. Axisymmetric and three-dimensional instabilities in an Ekman boundary layer flow. Intl J. Heat Fluid Flows 22, 82–93.

Schiestel, R., Elena, L., 1997. Modeling of anisotropic turbulence in rapid rotation. Aerospace Science and Technology 7, 441–451.

Schlichting, H., 1968. Boundary Layer Theory. Pergamon Press, London.

Schouveiler, L., Le Gal, P., Chauve, M.P., 2001. Instabilities of the flow between a rotating and a stationary disk. J. Fluid Mech. 443, 329–350.

Schuler, C.A., Usry, W.R., Weber, B., Humphrey, J.A.C., Greif, R., 1990. On the flow in the unobstructed space between shrouded corotating disks. Phys. Fluids A 2 (10), 1760–1770.

Tavener, S.J., Mullin, T., Cliffe, K.A., 1991. Novel bifurcation phenomena in a rotating annulus. J. Fluid Mech. 229, 483–497.

Tritton, D.J., 1988. Physical Fluid Dynamics. Clarendon Press, Oxford Science Publications, Oxford, UK.

Vanel, J.M., Peyret, R., Bontoux, P., 1986. A pseudospectral solution of vorticity-streamfunction equations using the influence matrix technique. In: Morton, K.W., Baines, M.J. (Eds.), Num. Meth. Fluid Dynamics II. Clarendon Press, pp. 463–475.